PHYSICAL REVIEW B **103**, 085408 (2021)

Higher-order topological Anderson insulators

Yan-Bin Yang,[1,*] Kai Li,[1,*] L.-M. Duan,[1] and Yong Xu[1,2,†]
[1]*Center for Quantum Information, IIS, Tsinghua University, Beijing 100084, People's Republic of China*
[2]*Shanghai Qi Zhi Institute, Shanghai 200030, People's Republic of China*

(Received 29 July 2020; revised 21 January 2021; accepted 22 January 2021; published 4 February 2021)

We study disorder effects in a two-dimensional system with chiral symmetry and find that disorder can induce a quadrupole topological insulating phase (a higher-order topological phase with quadrupole moments) from a topologically trivial phase. Their topological properties manifest in a topological invariant defined based on effective boundary Hamiltonians, the quadrupole moment, and zero-energy corner modes. We find gapped and gapless topological phases and a Griffiths regime. In the gapless topological phase, all the states are localized, while in the Griffiths regime, the states at zero energy become multifractal. We further apply the self-consistent Born approximation to show that the induced topological phase arises from disorder renormalized masses. We finally introduce a practical experimental scheme with topoelectrical circuits where the predicted topological phenomena can be observed by impedance measurements. Our work opens the door to studying higher-order topological Anderson insulators and their localization properties.

DOI: 10.1103/PhysRevB.103.085408

I. INTRODUCTION

Traditional topological phases usually feature the bulk-boundary correspondence that $(n-1)$-dimensional gapless boundary states exist for an n-dimensional topological system. Recently, topological phases have been generalized to the case where there exist $(n-m)$-dimensional [instead of $(n-1)$-dimensional] gapless boundary states with $1 < m \leqslant n$ for an n-dimensional system [1–3]. In the past few years, the higher-order topological phenomena have drawn tremendous attention, and various higher-order topological states have been discovered [1–14], such as quadrupole topological phases with zero-energy corner modes [1] and its type-II cousin [13] and second-order topological insulators with chiral hinge modes [7]. It has also been shown that higher-order topological insulators (HOTIs) are robust against weak disorder [15–20].

Disorder plays an important role in quantum transport, such as Anderson localization and metal-insulator transitions [21]. In the context of first-order topological phases, it has been shown that they are usually stable against weak symmetry preserving disorder. But disorder is not always detrimental to first-order topological phases. Reference [22] theoretically predicted that disorder can drive a topological phase transition from a metallic trivial phase to a quantum spin Hall insulator; topological insulators induced by disorder are called topological Anderson insulators (TAIs) [22,23]. Since their discovery, there has been great interest and advancement in the study of TAIs [24–29]. In addition, disorder can drive a transition from a Weyl semimetal to a three-dimensional (3D) quantum anomalous Hall state [30]. Remarkably, the TAI has been experimentally observed in a photonic waveguide array [31] and disordered cold atomic wire [32].

Disorder, topology, and symmetry are closely connected, which can be seen from classification theories. For example, random matrix theories are classified based on three internal symmetries, explaining universal transport properties of disordered physical systems [33–35]. Similarly, the classification of topological phases is made according to these internal symmetries [36]. Among these symmetries, chiral symmetry plays an important role in disordered systems and many peculiar properties have been found, such as the divergence of density of states (DOS) and localization length at energy $E = 0$ [37–41]. In two dimensions, first-order topological phases are not allowed in a system with only chiral symmetry. Yet, it has been reported that a second-order topological phase can exist in a two-dimensional (2D) system with chiral symmetry [42,43] and thus provides an ideal platform to study the interplay between disorder and topology.

Here we study the interplay between disorder and higher-order topology in a 2D system with chiral symmetry. We prove that the quantization of the quadrupole moment is maintained by chiral symmetry irrespective of crystalline symmetries, indicating that the quadrupole topological insulator can exist in a system with chiral symmetry without the requirement of any crystalline symmetry. This also gives us an opportunity to explore the effects of off-diagonal disorder respecting chiral symmetry. We theoretically predict the existence of a disorder-induced HOTI [dubbed higher-order topological Anderson insulator (HOTAI)] with zero-energy corner modes, which arises through the localization-delocalization-localization phase transition. We further apply the self-consistent Born approximation (SCBA) to show that the induced phase appears due to the disorder renormalized masses. Besides, we find gapped and gapless HOTAIs and a Griffiths regime. In the gapless regime, all the states are localized, while in the Griffiths regime, the states at zero energy become multifractal. In addition, we study the disorder effects on a HOTI and show the existence of gapped and

---

[*] These authors contributed equally to this work.

[†] yongxuphy@tsinghua.edu.cn

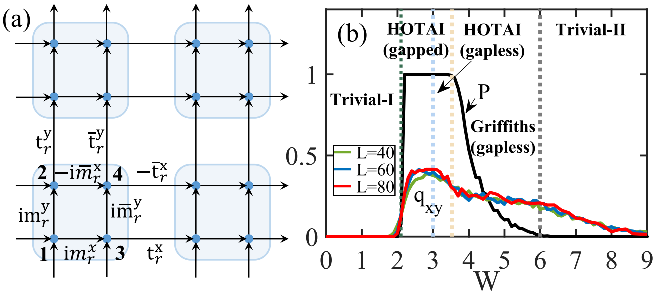

FIG. 1. (a) Schematics of our model (1). (b) The phase diagram with respect to the disorder strength W mapped out based on the topological invariant P, the quadrupole moments q_{xy}, and the bulk energy gap shown in Fig. 2(a). We observe distinct phases including gapped and gapless HOTAI, Griffiths phase, and trivial I and II phases, separated by vertical dashed lines. Here $m_x = m_y = 1.1$.

gapless topological phases and a Griffiths regime. Finally, we propose an experimental scheme using topoelectrical circuits to realize and detect the HOTAI.

II. MODEL HAMILTONIAN

We start by considering the following higher-order Hamiltonian:

$$\hat{H} = \sum_{\mathbf{r}} [\hat{c}_{\mathbf{r}}^\dagger h_0 \hat{c}_{\mathbf{r}} + (\hat{c}_{\mathbf{r}}^\dagger h_x \hat{c}_{\mathbf{r}+\mathbf{e}_x} + \hat{c}_{\mathbf{r}}^\dagger h_y \hat{c}_{\mathbf{r}+\mathbf{e}_y} + \text{H.c.})], \tag{1}$$

where $\hat{c}_{\mathbf{r}}^\dagger = (\hat{c}_{\mathbf{r}1}^\dagger \quad \hat{c}_{\mathbf{r}2}^\dagger \quad \hat{c}_{\mathbf{r}3}^\dagger \quad \hat{c}_{\mathbf{r}4}^\dagger)$ with $\hat{c}_{\mathbf{r}\nu}^\dagger$ ($\hat{c}_{\mathbf{r}\nu}$) being a creation (annihilation) operator at the νth site in a unit cell described by $\mathbf{r} = (x, y)$ with x and y being integers (suppose that the lattice constants are equal to one), $\mathbf{e}_x = (1, 0)$ and $\mathbf{e}_y = (0, 1)$. Here

$$h_0 = \begin{pmatrix} 0 & -im_{\mathbf{r}}^y & -im_{\mathbf{r}}^x & 0 \\ im_{\mathbf{r}}^y & 0 & 0 & i\bar{m}_{\mathbf{r}}^x \\ im_{\mathbf{r}}^x & 0 & 0 & -i\bar{m}_{\mathbf{r}}^y \\ 0 & -i\bar{m}_{\mathbf{r}}^x & i\bar{m}_{\mathbf{r}}^y & 0 \end{pmatrix} \tag{2}$$

depicts the intracell hopping, and

$$h_x = \begin{pmatrix} 0 & 0 & 0 & 0 \\ 0 & 0 & 0 & 0 \\ t_{\mathbf{r}}^x & 0 & 0 & 0 \\ 0 & -\bar{t}_{\mathbf{r}}^x & 0 & 0 \end{pmatrix} \text{and } h_y = \begin{pmatrix} 0 & 0 & 0 & 0 \\ t_{\mathbf{r}}^y & 0 & 0 & 0 \\ 0 & 0 & 0 & 0 \\ 0 & 0 & \bar{t}_{\mathbf{r}}^y & 0 \end{pmatrix} \tag{3}$$

describe the intercell hopping along x and y, respectively [also see Fig. 1(a) for the hopping parameters]. The system parameters $m_{\mathbf{r}}^x$, $\bar{m}_{\mathbf{r}}^x$, $m_{\mathbf{r}}^y$, $\bar{m}_{\mathbf{r}}^y$, $t_{\mathbf{r}}^x$, $\bar{t}_{\mathbf{r}}^x$, $t_{\mathbf{r}}^y$, and $\bar{t}_{\mathbf{r}}^y$ all take real values. For simplicity without loss of generality, we take the intercell hopping magnitude as energy units so that $t_{\mathbf{r}}^x = \bar{t}_{\mathbf{r}}^x = t_{\mathbf{r}}^y = \bar{t}_{\mathbf{r}}^y = 1$. In this case, $h_x = \sigma_- \otimes \sigma_z$ and $h_y = \sigma_0 \otimes \sigma_-$ with $\sigma_- = [0\,0; 1\,0]$ and σ_0 being a 2×2 identity matrix. For a clean system with $m_{\mathbf{r}}^x = \bar{m}_{\mathbf{r}}^x = m_{\mathbf{r}}^y = \bar{m}_{\mathbf{r}}^y = m$, the system respects a generalized C_4 symmetry as detailed in Appendix A.

To show that Hamiltonian (1) describes a higher-order phase supporting zero-energy corner modes in the clean case with $m_{\mathbf{r}}^x = \bar{m}_{\mathbf{r}}^x = m_x$ and $m_{\mathbf{r}}^y = \bar{m}_{\mathbf{r}}^y = m_y$, we write the Hamiltonian in momentum space as

$$\hat{H} = \sum_{\mathbf{k}} \hat{c}_{\mathbf{k}}^\dagger H_0(\mathbf{k}) \hat{c}_{\mathbf{k}}. \tag{4}$$

Here

$$H_0(\mathbf{k}) = H_x(k_x, m_x) \otimes \sigma_z + \sigma_0 \otimes H_y(k_y, m_y), \tag{5}$$

where $H_\nu(k_\nu, m_\nu) = \cos k_\nu \sigma_x + (m_\nu + \sin k_\nu)\sigma_y \quad (\nu = x, y)$ with $\sigma_\nu (\nu = x, y, z)$ being the Pauli matrices and σ_0 being a 2×2 identity matrix. To see the presence of zero-energy corner modes in the system, we recast Hamiltonian (5) to a form in continuous real space by replacing $\sin k_\nu$ by $-i\partial_\nu$ and $\cos k_\nu$ by $1 + \partial_\nu^2/2$ $(\nu = x, y)$ so that $H_\nu(k_\nu) \rightarrow \bar{H}_\nu$. Considering semi-infinite boundaries along x and y, if $|u_x\rangle$ and $|u_y\rangle$ are zero-energy edge modes of $\bar{H}_x$ and $\bar{H}_y$, respectively, $|u_x\rangle \otimes |u_y\rangle$ is a zero-energy mode of $\bar{H}_0$ localized at a corner.

Since the system contains only the nearest-neighbor hopping, it respects chiral symmetry, i.e., $\Pi H \Pi^{-1} = -H$, where H is the first-quantization Hamiltonian and Π is a unitary matrix. But this system breaks the time-reversal symmetry and thus the particle-hole symmetry, because h_0 is complex. In contrast, if we generalize the Benalcazar-Bernevig-Hughes (BBH) model [1] to the disordered case, it still respects the time-reversal, particle-hole, and chiral symmetries. However, these two models are connected through a local transformation and thus have similar topological and localization properties as proved in Appendix B. The equivalence also tells us that our system supports zero-energy corner modes and has quantized quadrupole moments [44,45] protected by reflection symmetries. But with disorder breaking the reflection symmetry, one may wonder whether the quadrupole moment is still quantized. Here we prove the quantization of the quadrupole moment maintained by chiral symmetry (see Appendix C), indicating that chiral symmetry can protect a quadrupole topological insulator. We remark that in three dimensions chiral symmetry maintains the quantization of the octupole moment as proved in Appendix C, indicating that chiral symmetry can protect the third-order topological insulator with zero-energy corner modes in three dimensions.

To study the disorder effects, we consider the disorder in the intracell hopping, that is, $m_{\mathbf{r}}^\nu = m_\nu + W^\nu V_{\mathbf{r}}^\nu$ and $\bar{m}_{\mathbf{r}}^\nu = m_\nu + \bar{W}^\nu \bar{V}_{\mathbf{r}}^\nu$ with $\nu = x, y$, where $V_{\mathbf{r}}^\nu$ and $\bar{V}_{\mathbf{r}}^\nu$ are uniformly randomly distributed in $[-0.5, 0.5]$ without correlation. Here W^ν and $\bar{W}^\nu$ represent the disorder strength. For simplicity, we take $W^x = \bar{W}^x = W^y = \bar{W}^y = W$. Because of the random character, we perform the average over 200 to 2000 sample configurations for numerical calculation.

III. HIGHER-ORDER TOPOLOGICAL ANDERSON INSULATORS

We map out the phase diagram in Fig. 1(b), showing remarkably the presence of a disorder-induced higher-order topological phase transition. To characterize the phase transition, we evaluate the polarization p_x (p_y) of effective boundary Hamiltonians at a y-normal (x-normal) boundary at half filling. In one dimension, the polarization is equivalent to the Berry phase in a translation-invariant system, which can be used as a topological invariant [46]. In fact, the polarization as a topological invariant can be evaluated in real space for a system without translational symmetries based on Resta's formula [27,46]. For the quadrupole topological phase, we define a topological invariant based on p_x and p_y as

$$P = 4|p_x p_y|. \tag{6}$$

When $P = 1$, the system is in a higher-order topologically nontrivial phase, and when $P = 0$, it is in a trivial phase (see Appendix D for its justification for a clean system).

We now generalize it to the disordered case. Specifically, we evaluate the average polarization of the effective boundary Hamiltonian at the y-normal boundary (similarly for x-normal one) by $p_x = \frac{1}{N_i}\sum_{n=1}^{N_i}|p_{x,n}|$, where $p_{x,n} = \mathrm{Im}\log\langle\Psi_n|e^{2\pi i\hat{x}/L_x}|\Psi_n\rangle/(2\pi)$ [46] with $\hat{x} = \sum_x x\hat{n}_x$, $\hat{n}_x$ being the particle number operator at the site x, and L_x being the length of the system along x (we also deduct the atomic positive charge contribution). Here $|\Psi_n\rangle$ is the ground state at half filling of the boundary Hamiltonian $H_n = -G_{2n}(E=0)^{-1}$ with G_{2n} being the $2n$th boundary Green's function obtained by [47,48]

$$G_n = (E - h_n - V_{n-1}G_{n-1}V_{n-1}^{\dagger})^{-1}, \tag{7}$$

where h_n is the Hamiltonian for the nth layer and V_{n-1} is the coupling between the $(n-1)$th and nth layers. We note that $p_{x,n}$ is quantized to be either zero or 0.5 for each iteration since H_n also preserves chiral symmetry. The polarization is evaluated at even steps of Green's function given that there are two different layers in the clean limit. In the disordered case, the intracell hopping parts in h_n and V_n are randomly generated for each iteration (see Appendix D). The topological invariant P is finally determined.

In Fig. 1(b), we plot the topological invariant P as the disorder magnitude increases. We see that P suddenly jumps to 1 when $W \approx 2.1$, indicating the occurrence of a topological phase transition. P remains quantized to be 1 until $W > 3.5$, where it begins decreasing continuously. This regime corresponds to the Griffiths phase where topologically trivial and nontrivial sample configurations coexist (see Appendix E). When $W > 6$, P vanishes, showing that the system reenters into a trivial phase.

To further identify that the induced topological phase is a quadrupole topological phase, we calculate the quadrupole moment, which can be used as a topological invariant since its quantization is protected by chiral symmetry (see Appendix C). Figure 1(b) shows that the quadrupole moment qualitatively agrees with the results of P. Yet, conspicuous discrepancy can be observed. The quadrupole moment q_{xy} over many samples is not quantized to 0.5 in the regime where $P = 1$ [$q_{xy} = 0.5$ for most disorder configurations and $q_{xy} = 0$ for other configurations (see Fig. 9 in Appendix C)] and the Griffiths regime is much larger. We attribute this to the finite-size effects, given that for the quadrupole moment, we can only perform a computation for a system with its size up to 80, while to determine P, we consider a system with its size up to 500 and iterations up to 10^3. To be more quantitative, we plot $0.5 - q_{xy}$ as the system size L increases when $W = 2.6$ in Fig. 2(b), showing a power-law decay and thus suggesting that q_{xy} approaches 0.5 in the thermodynamic limit.

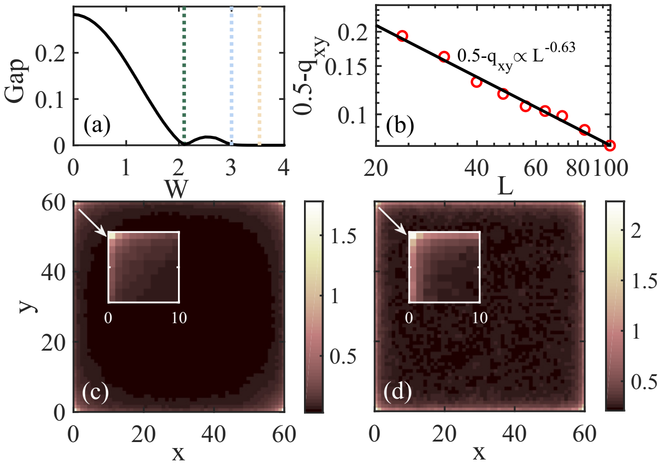

FIG. 2. (a) The bulk energy gap versus W. (b) The quadrupole moment (red circles) versus the system size L when $W = 2.6$, which is fitted by a power-law function plotted as the black line. The zero-energy local density of states (LDOS) obtained under open boundary conditions for (c) $W = 2.6$ and (d) $W = 3.4$. The zoomed-in view of the LDOS around one corner is shown in the insets. Here $m_x = m_y = 1.1$.

The higher-order topological phase transition occurs as the bulk energy gap closes at $W \approx 2.1$ and reopens, as shown in Fig. 2(a). In fact, the transition is associated with the divergence of the localization length at $W \approx 2.1$ [see Fig. 3(a)]. When W is further increased, the energy gap closes again and remains closed due to the strong disorder scattering, leading to the gapless HOTAI. Even in the gapless regime, the topological invariant P can still be quantized as shown in Fig. 1(b). In fact, in this phase, all the states are localized, corresponding to an Anderson insulator (see the following discussion).

To further confirm that the TAI is a higher-order topological state, in Figs. 2(c) and 2(d) we display the local density of states (LDOS) at $E = 0$ for two typical values of W corresponding to a gapped and gapless topological phase, respectively, clearly showing the presence of zero-energy states localized at corners. The evidence above definitely suggests the existence of HOTAIs.

IV. LOCALIZATION PROPERTIES

We now study the localization properties of energy bands in different phases by evaluating their localization length, adjacent level-spacing ratio (LSR), inverse participation ratio (IPR), and fractal dimensions. The LSR is defined as

$$r(E) = \left[\frac{1}{N_E - 2}\sum_i \min(\delta_i, \delta_{i+1})/\max(\delta_i, \delta_{i+1})\right], \tag{8}$$

where $\delta_i = E_i - E_{i-1}$ with E_i being the ith eigenenergy sorted in an ascending order and $\sum_i$ denotes the sum over an energy bin around the energy E with N_E energy levels counted. For localized states, $r \approx 0.386$ corresponds to the Poisson statistics, and for extended states of symmetric real Hamiltonians,

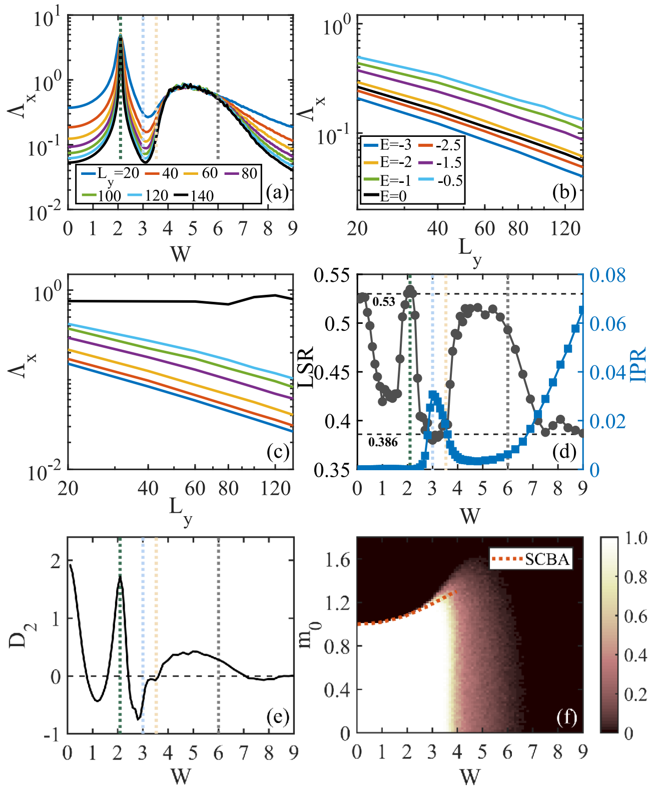

FIG. 3. (a) The normalized localization length Λ_x at $E = 0$ versus W for several distinct L_y. The scaling of Λ_x at different energies for (b) $W = 3.2$ and (c) $W = 4.6$. (d) The level-spacing ratio (LSR) and inverse participation ratio (IPR) versus W for the eigenstates around zero energy in a system with size $L = 500$. (e) The fractal dimension D_2 with respect to W for the eigenstates around zero energy. The vertical dashed lines separate different phases. (f) The topological invariant P in the (W, m_0) plane with $m_0 = m_x = m_y$. The red dotted line indicates the topological phase boundary determined by the SCBA. In [(a)–(e)], $m_x = m_y = 1.1$.

$r \approx 0.53$ corresponds to the Gaussian orthogonal ensemble (GOE) [49].

The localization property can also be characterized by the real-space IPR defined as

$$I(E) = \left[\frac{1}{N_E}\sum_i\sum_{\mathbf{r}}\left(\sum_{\nu=1}^{4}|\Psi_{E_i,\mathbf{r}\nu}|^2\right)^2\right]. \qquad (9)$$

This quantity evaluates how much a state in an energy bin around energy E is spatially localized. For an extended state in two dimensions, $I \propto 1/L^2$ with L being the size of a system, which goes to zero in the thermodynamic limit; for a state localized in a single unit cell, it is one. It is well known that at the critical point between localized and delocalized phases, the state exhibits multifractal behavior with fractal dimensions D_2 defined through $I \propto 1/L^{D_2}$ [50]. Clearly, $D_2 = 2$ and $D_2 = 0$ indicate that a state is extended and localized, respectively, in the thermodynamic limit; intermediate values of D_2 suggests the multifractal state.

In Fig. 3(a), we plot the normalized localization length $\Lambda_x = \lambda_x/L_y$ (similarly for λ_y/L_x) with respect to the disorder strength W at $E = 0$ for distinct L_y, where λ_ν ($\nu = x, y$) is the localization length along ν calculated by the transfer matrix method [51]. In the gapless HOTAI and trivial-II phases, we see the decrease of Λ_x as L_y is increased, suggesting that the states at $E = 0$ are localized. The decline can also be clearly seen in Fig. 3(b) where Λ_x versus L_y is plotted for $W = 3.2$ for distinct energies. In fact, all states are localized in these two phases as detailed in the following discussion. This shows that even in the higher-order case, the topology can be carried by localized bulk states. Being localized for the states in these regimes is also evidenced by their relatively large IPR and the LSR approaching 0.386 [see Fig. 3(d)]. In these regimes, the fractal dimension D_2 becomes negative or approaches zero [see Fig. 3(e)], further indicating that the states around zero energy are localized. We note that the negative D_2 arises from finite-size effects. It indicates that the IPR rises with increasing the system size, suggesting that the states are localized (see Appendix F for the finite-size analysis).

Figure 3(a) also demonstrates the existence of a regime (corresponding to the Griffiths regime) where Λ_x at $E = 0$ remains almost unchanged as L_y increases, suggesting a multifractal phase in this regime. The multifractal phase resides between two localized phases, which is very different from the conventional wisdom that a multifractal phase lives at the critical point between delocalized and localized phases. In fact, only the states at or very near $E = 0$ become multifractal, and all other states remain localized [see Fig. 3(c)]. The multifractal properties are also evidenced by the fractal dimension of the states around zero energy as shown in Fig. 3(e).

In the gapped regime, there are trivial-I and gapped HOTAI phases. In the trivial phase, the states at the band edge around zero energy exhibit the LSR close to 0.386 [see Fig. 3(d)], suggesting the localized property of these states. The localized property is also evidenced by the negative D_2 (in the region around $W = 1$) [see Fig. 3(e)]. We note that near the phase-transition points of $W = 0$ and $W = 2.1$, the states exhibit delocalized properties due to the large localization length. In the gapped HOTAI, Figs. 3(d) and 3(e) illustrate that the LSR experiences a drop from around 0.53 to 0.386 and D_2 drops from 1.72 to negative values, suggesting that the states at the band edge undergo a phase transition from delocalized to localized ones.

The above results indicate that, for strong disorder, all states are localized in the gapless HOTAI and the trivial-II phase. Yet in the Griffiths phase, all states are localized except at $E = 0$ where the states become multifractal. For weak disorder, all states can be localized in the topological regime. In the trivial-I phase, the states at the band edge around zero energy are localized.

In the following, we provide more evidence on localization properties. Figure 4 shows the LSR as a function of energy for five different disorder amplitudes. For small W corresponding to the trivial-I phase [Fig. 4(a) and its inset], the LSR remains around 0.53 except at the lower band edge where it exhibits a sudden drop towards 0.386, indicating that the states at the band edge are localized. But we cannot claim the existence of mobility edges in the trivial-I phase given that it is very possible that the delocalized behavior is caused by the finite-size effects, which is very difficult to identify since the localization length is huge for the weak disorder. In the

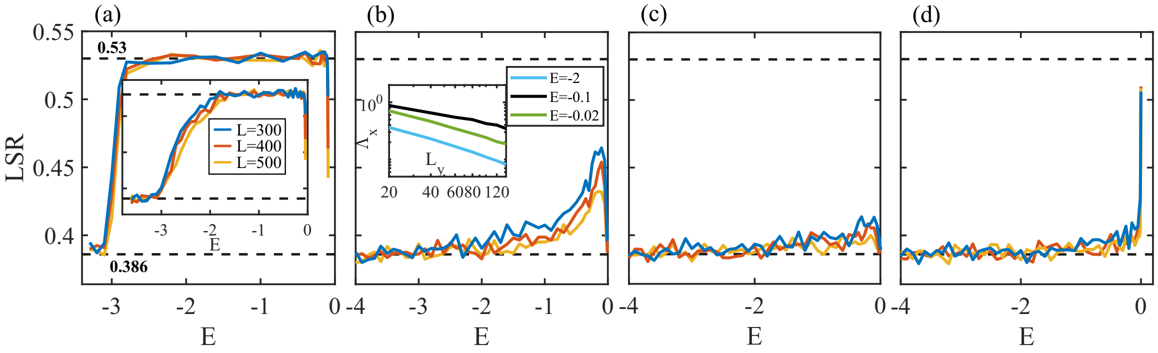

FIG. 4. The LSR versus energy E for (a) $W = 1$, (b) $W = 2.8$, (c) $W = 3.2$, and (d) $W = 4.6$ in the trivial-I, gapped HOTAI, gapless HOTAI, and Griffiths phases, respectively. The blue, red, and yellow lines describe results for the system size $L_x = L_y = L = 300$, 400, and 500, respectively. The inset in (a) displays the LSR as a function of E for $W = 1.5$. The inset in (b) shows the normalized localization length Λ_x with respect to L_y at different energies. Here $m_x = m_y = 1.1$.

gapped HOTAI, while we cannot conclusively determine that all states are localized when W is near the transition point, we show that this occurs when W is larger. For instance, when $W = 2.8$, Fig. 4(b) illustrates that the LSR decreases towards 0.386 with the increase of the system size. We also plot the normalized localization length with respect to L_y for different energies, the fall of which clearly suggests that the states are localized. These indicators show that all the states are localized. Similarly, Fig. 4(c) indicates that all the states are localized in the gapless HOTAI phase. But in the Griffiths regime, all the states are localized except at $E = 0$ where the LSR remains unchanged as the system size is increased [see Fig. 4(d)].

We also compute the DOS at $E = 0$ with respect to the disorder strength W as shown in Fig. 5(a). The DOS is defined as $\rho(E) = \sum_{\mathbf{r}} \rho(E, \mathbf{r})/(4L_xL_y)$, which is normalized to one, i.e., $\int dE\,\rho(E) = 1$. Here $\rho(E, \mathbf{r}) = [\sum_j \delta(E - E_j) \sum_{\nu=1}^{4} |\Psi_{E_j,\mathbf{r}\nu}|^2]$ describes the LDOS, where $\Psi_{E_i,\mathbf{r}\nu}$ denotes the spatial eigenstate of the system with periodic boundaries corresponding to the eigenenergy E_i, and $[\cdots]$ denotes the average over different samples. The DOS rises to the maximum in the multifractal phase and then falls in the trivial-II phase. Specifically, we see the development of a very narrow peak of the DOS at $E = 0$ in this regime [Fig. 5(b)].

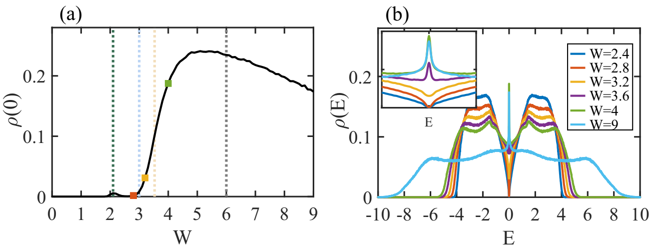

FIG. 5. (a) The DOS at zero energy $\rho(0)$ versus the disorder strength W calculated by the kernel polynomial method (KPM) for the system size $L = 100$ and the expansion order $N_c = 2^{13}$. (b) The DOS $\rho(E)$ versus E for different W with the zoomed-in view around zero energy in the inset. The vertical dashed lines separate different phases. Here $m_x = m_y = 1.1$.

V. SELF-CONSISTENT BORN APPROXIMATION

We now explain the disorder-induced quadrupole topological insulator based on the SCBA [23]. As introduced in Sec. II, we consider a disordered system by adding the following random intracell hopping terms at each unit cell $\mathbf{r}$:

$$V(\mathbf{r}) = W \begin{pmatrix} 0 & -iV_3(\mathbf{r}) & -iV_1(\mathbf{r}) & 0 \\ iV_3(\mathbf{r}) & 0 & 0 & iV_2(\mathbf{r}) \\ iV_1(\mathbf{r}) & 0 & 0 & -iV_4(\mathbf{r}) \\ 0 & -iV_2(\mathbf{r}) & iV_4(\mathbf{r}) & 0 \end{pmatrix}$$

$$= W[V_1'(\mathbf{r})U_1 + V_2'(\mathbf{r})U_2 + V_3'(\mathbf{r})U_3 + V_4'(\mathbf{r})U_4], \quad (10)$$

where $V_1' = (V_1 + V_2)/2$, $V_2' = (V_1 - V_2)/2$, $V_3' = (V_3 + V_4)/2$, $V_4' = (V_3 - V_4)/2$, and $U_1 = \sigma_y \otimes \sigma_z$, $U_2 = \sigma_y \otimes \sigma_0$, $U_3 = \sigma_0 \otimes \sigma_y$, $U_4 = \sigma_z \otimes \sigma_y$. Here we have changed the notation in Sec. II by $V^x \to V_1$, $\bar{V}^x \to V_2$, $V^y \to V_3$, and $\bar{V}^y \to V_4$ for convenience. Since we are interested in disorder without correlations, we require

$$\langle V_i'(\mathbf{R}) \rangle = 0, \quad (11)$$

$$\langle V_i'(\mathbf{R}_1)V_j'(\mathbf{R}_2) \rangle = \frac{1}{24}\delta_{ij}\delta_{\mathbf{R}_1\mathbf{R}_2}, \quad (12)$$

for $i, j = 1, 2, 3, 4$ with $\langle \cdots \rangle$ denoting the average over disorder ensembles.

Based on the self-consistent Born approximation, the effective Hamiltonian at $E = 0$ is given by $H_{\text{eff}}(\mathbf{k}) = H_0(\mathbf{k}) + \Sigma(E = 0)$ where the self-energy Σ in the presence of disorder can be calculated through the following self-consistent equation:

$$\Sigma(E) = \frac{W^2}{96\pi^2} \int_{BZ} d^2\mathbf{k} \sum_{n=1}^{4} U_n G U_n, \quad (13)$$

where $G = [(E + i0^+)I - H_0(\mathbf{k}) - \Sigma(E)]^{-1}$. At energy $E = 0$, we find numerically that the self-energy can be expanded as

$$\Sigma = i\Sigma_0 I + \Sigma_x \sigma_y \otimes \sigma_z + \Sigma_y \sigma_0 \otimes \sigma_y, \quad (14)$$

with Σ_0, Σ_x, Σ_y being real numbers. It is clear to see that the topological masses m_x and m_y associated with topological properties are renormalized by disorder to new values

$$m_x' = m_x + \Sigma_x, \quad (15)$$

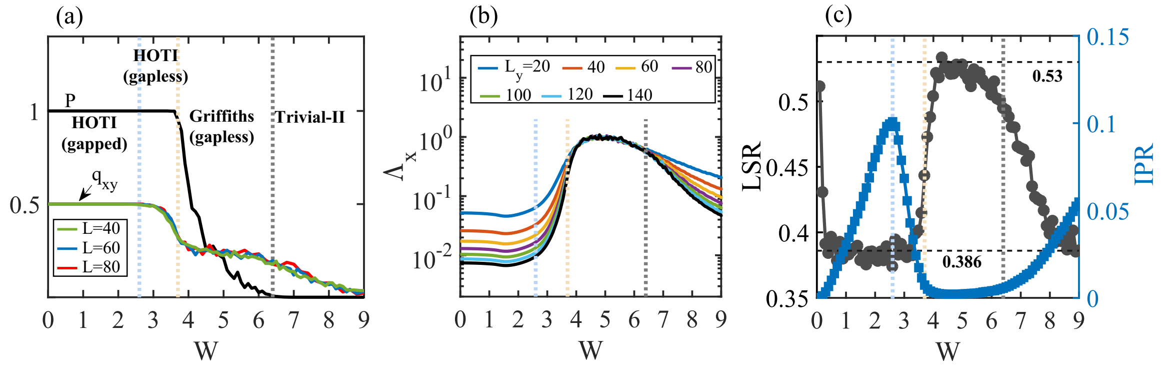

FIG. 6. (a) The phase diagram with respect to W, where P and the quadrupole moments are displayed. Here the gapped and gapless HOTI, the Griffiths phase, and the trivial-II phase are observed. (b) Λ_x at $E = 0$ versus W for different L_y. (c) The LSR and IPR versus W for the eigenstates around zero energy of a system with $L = 200$. The vertical dashed lines separate different phases. Here $m_x = m_y = 0.5$.

$$m'_y = m_y + \Sigma_y. \tag{16}$$

Based on Eq. (13), we first approximate the self-energy Σ by taking $\Sigma = 0$ in the right-hand side of the equation, yielding

$$\Sigma_\nu = -\frac{W^2}{48\pi^2}\iint_{BZ} d\mathbf{k} I_\nu, \tag{17}$$

where

$$I_\nu = \frac{m_\nu + \sin(k_\nu)}{F(\mathbf{k})}, \tag{18}$$

$$F(\mathbf{k}) = 2 + \sum_{\nu=x,y}\left[m_\nu^2 + 2m_\nu \sin(k_\nu)\right], \tag{19}$$

with $\nu = x, y$. When $m_x > 1$ and $m_y > 1$, both Σ_x and Σ_y are negative due to the positive integrands, leading to a topological phase transition when the disorder strength W is sufficiently large so that $m'_x < 1$ and $m'_y < 1$. We also numerically solve Eq. (13) self-consistently to determine Σ_x and Σ_y and plot the results in Fig. 3(f). For weak disorder, the results agree very well with the numerical phase boundary.

VI. DISORDER EFFECTS ON HOTIS

In this section, we study the effects of disorder on HOTIs. Specifically, we consider $m_x = m_y = 0.5$ corresponding to a HOTI in the clean limit. We find that the topological phase is stable against weak disorder as evidenced by the quantized topological invariant P in Fig. 6(a). When the disorder strength becomes sufficiently strong, it enters into a Griffiths regime with fractional P and finally becomes a trivial phase. The strong disorder also closes the energy gap when $W > 2.6$. In the gapless HOTI and trivial-II phases, all states are localized, as evidenced by the normalized localization length, LSR, and IPR [see Figs. 6(b) and 6(c)]. In the Griffiths regime, the states at $E = 0$ are multifractal and all other states are localized [see Fig. 6(b)]. In the disordered gapped HOTI, we find that for weak disorder, the states near the band edge are localized as shown by the LSR around 0.386 in Fig. 6(c). For larger disorder, all the states become localized in this phase.

Figure 7 further plots the LSR with respect to E for four different disorder strengths. When the disorder is weak, e.g., $W = 1$, the LSR shows that the states near the band edge are localized in the gapped HOTI [Fig. 7(a)]. Yet, when $W = 2$, the LSR of all the states decreases towards 0.386 with the increase of the system size, reflecting that all the states are localized. The localized property is also signaled by the decline of the normalized localization length with increasing L_y [Fig. 7(b)]. Similarly, in the gapless HOTI, all the states are localized as shown in Fig. 7(c). In this case, the LSR at $E = -1$ decreases towards 0.386 as the system size is increased, providing further evidence for localization. In the Griffiths regime, the LSR becomes smaller for larger system sizes except at $E = 0$ where it remains unchanged, suggesting that the states at $E = 0$ are multifractal and all other states are localized. The multifractal property is also reflected by the unchanged property of the normalized localization length as L_y is increased [Fig. 7(d)].

VII. EXPERIMENTAL REALIZATION

The BBH model has been experimentally realized in several metamaterials, such as microwave, phononic, photonic, and topoelectrical circuit systems [52–55]. In fact, some systems, such as silicon ring resonators [55], have demonstrated the robustness of zero-energy corner modes to certain disorders. The HOTAI can be easily realized in these systems when the off-diagonal hopping disorder is considered in the experimentally realized BBH model. The BBH model has also been implemented in topoelectrical circuits, and zero-energy corner modes are probed by measuring two-point impedances [54]. One can involve disorder in the system by tuning the capacitance of capacitors and inductance of inductors to realize the HOTAI, as we have proved that this model is equivalent to our model in topological and localization properties (see Appendix B). In the following, we discuss in detail an experimental scheme to realize the Hamiltonian (1) using topoelectrical circuits and show that the HOTAI phase can be detected by two-point impedance measurements.

Let us consider an electric network composed of different nodes and electric element connecting nodes, as shown in Fig. 8(a). We denote the input current and voltage of each node a by I_a and V_a, respectively. According to Kirchhoff's

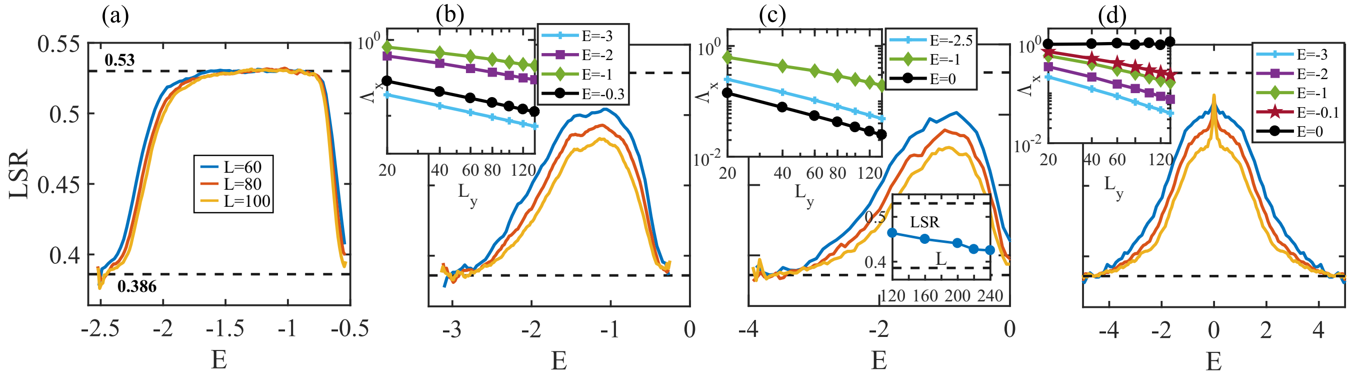

FIG. 7. The LSR versus energy E for (a) $W = 1$, (b) $W = 2$, (c) $W = 3.2$, and (d) $W = 5$ in gapped HOTI, gapless HOTI, and Griffiths phase, respectively. The top insets in (b), (c), and (d) describe the normalized localization length Λ_x with respect to L_y at different energies. The bottom inset in (c) plots the LSR as a function of system size L at $E = -1$. Here $m_x = m_y = 0.5$.

law, the circuit at a frequency of ω should satisfy the relation

$$I_a(\omega) = \sum_b R_{ab}(V_a(\omega) - V_b(\omega)) + R_a V_a(\omega), \tag{20}$$

where R_{ab} is the admittance of the corresponding electric element between the node a and b, and R_a is the admittance of the electric element between the node a and the ground. We can rewrite the above equation into a compact form as

$$\mathbf{I}(\omega) = J(\omega)\mathbf{V}(\omega), \tag{21}$$

where $\mathbf{I}$ and $\mathbf{V}$ are N-component column vectors with components I_a and V_a for N nodes, respectively. Here the matrix J is the circuit Laplacian. Then we can simulate our Hamiltonian H with the Laplacian $J(\omega)$ at a proper frequency ω through

$$J(\omega) = iH. \tag{22}$$

Each node in the circuit represents one lattice site in our Hamiltonian, and each electric element linking two nodes represents the corresponding hopping between the sites, which can be a capacitor, or an inductor, or a negative impedance converter with current inversion (INIC). For two nodes in the circuit, the electric element between them is determined according to the corresponding matrix element H_{ab} between the site a and b in our Hamiltonian, as illustrated in Fig. 8(a). Specifically, for two neighboring sites in our Hamiltonian, if H_{ab} is a positive (negative) real number, the electric element between a and b should be an inductor (a capacitor) with inductance (capacitance) $\frac{1}{\omega H_{ab}}$ $(-\frac{H_{ab}}{\omega})$. For the case that H_{ab} is an imaginary number, we should connect the two nodes using an INIC with resistance $\frac{1}{|H_{ab}|}$ and proper direction. In addition, we connect every node with the ground by appropriate electric elements to eliminate the extra diagonal terms in the Laplacian.

Similar to the experimental work [54], we utilize the two-point impedance measurement in the circuit to characterize the zero-energy corner modes in the HOTAI phase. The two-point impedance between node a and b is defined as

$$Z_{ab} = \sum_n \frac{|\psi_{n,a} - \psi_{n,b}|^2}{j_n}, \tag{23}$$

where $\psi_{n,a}$ is the component for node a of the nth eigenvector of J with eigenvalue j_n. We define the impedance of each

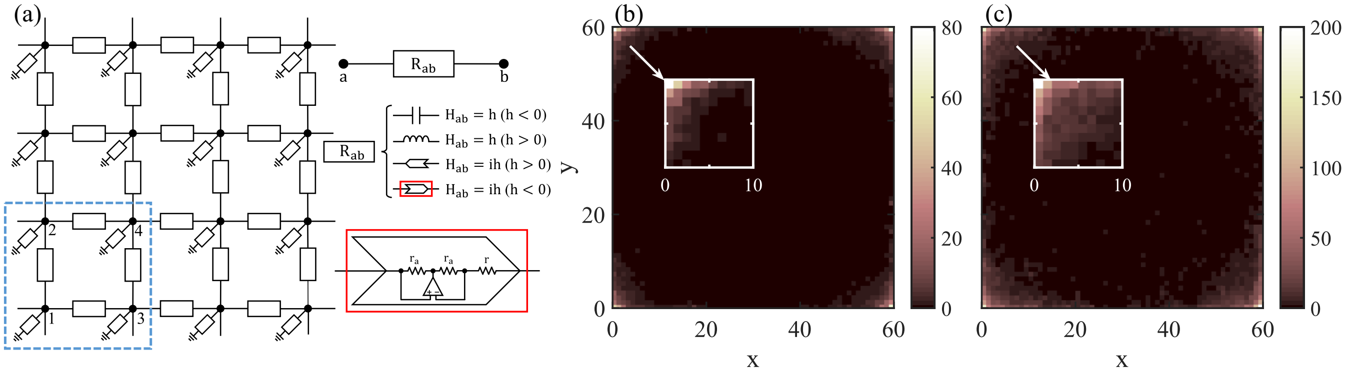

FIG. 8. (a) Schematics of an electric network for realizing our Hamiltonian (1). Here each node in the circuit represents one lattice site in the Hamiltonian, and four nodes form a unit cell as shown in the blue dashed box. The hopping between two neighboring sites H_{ab} is simulated by the admittance R_{ab} of the electric element connecting them. The different values of H_{ab} correspond to different electric elements, including capacitors, inductors, or negative impedance converters with current inversion (INICs) whose structure is shown in the red box. Each node a should be grounded through an electric element with an appropriate admittance R_a. [(b),(c)] The averaged magnitude of the impedance $|Z(x, y)|$ of each unit cell under open boundary conditions for $W = 2.6$ and $W = 3.4$, respectively. The insets show the zoomed-in view of $|Z(x, y)|$ around one corner. Here $m_x = m_y = 1.1$.

unit cell, $Z(x, y)$, as the average two-point impedance between nearest-neighbor nodes within each unit cell,

$$Z(x,y) = \frac{Z_{12}(x,y) + Z_{24}(x,y) + Z_{43}(x,y) + Z_{31}(x,y)}{4}, \tag{24}$$

where $Z_{ij}(x, y)$ denotes the two-point impedance between the ith node and jth node of the unit cell (x, y). Figures 8(b) and 8(c) plot the magnitude of $Z(x, y)$ averaged over 400 random samples under open boundary conditions for two values of W within the HOTAI regime for $m_x = m_y = 1.1$, which clearly shows the impedance resonance near the corners corresponding to the presence of zero-energy corner modes of the Hamiltonian.

VIII. CONCLUSION

In summary, we have discovered the HOTAI in a 2D disordered system with chiral symmetry. Specifically, we show that a topologically trivial phase can transition into a quadrupole topological phase when disorder is added. We find gapped and gapless HOTAIs and a Griffiths regime. In the gapless HOTAI, all the states are localized, while in the Griffiths regime, the states at zero energy are multifractal and other states are localized. The Griffiths regime corresponds to a critical regime between two localized phases: a gapless HOTAI and a trivial phase. We also propose an experimental scheme with topoelectrical circuits to realize the HOTAI. Our results demonstrate that disorder can induce quadrupole topological insulators with peculiar localization properties from a trivial phase and thus opens an avenue for studying the role of disorder in higher-order topological phases.

Note added. Recently, we became aware of two related works [56,57].

ACKNOWLEDGMENTS

We thank Y.-L. Tao and N. Dai for helpful discussion. Y.B.Y., K.L., and Y.X. are supported by the National Natural Science Foundation of China (Grant No. 11974201), the startup fund from Tsinghua University and the National Thousand-Young-Talents Program. We acknowledge in addition support from the Frontier Science Center for Quantum Information of the Ministry of Education of China, Tsinghua University Initiative Scientific Research Program, and the National Key Research and Development Program of China (Grant No. 2016YFA0301902).

APPENDIX A: GENERALIZED C_4 SYMMETRY

In the clean case, when $m_x = m_y$ and $t_x = t_y$, Hamiltonian (1) in the main text respects a generalized C_4 symmetry,

$$U_{C_4} \hat{H} U_{C_4}^{-1} = \hat{H}, \tag{A1}$$

where

$$U_{C_4} \hat{c}_{\mathbf{r}} U_{C_4}^{-1} = S_{\mathbf{r}} \hat{c}_{g\mathbf{r}}, \quad U_{C_4} \hat{c}_{\mathbf{r}}^\dagger U_{C_4}^{-1} = \hat{c}_{g\mathbf{r}}^\dagger S_{\mathbf{r}}^T, \tag{A2}$$

with

$$S_{\mathbf{r}} = \begin{pmatrix} 0 & 0 & (-1)^y & 0 \\ -(-1)^y & 0 & 0 & 0 \\ 0 & 0 & 0 & (-1)^y \\ 0 & (-1)^y & 0 & 0 \end{pmatrix} \tag{A3}$$

and g being a C_4 rotation operator such that $g\mathbf{r} = (-y, x)$.

In momentum space, let us write $\hat{H} = \sum_{\mathbf{k}} \hat{c}_{\mathbf{k}}^\dagger H(\mathbf{k}) \hat{c}_{\mathbf{k}}$ with $\hat{c}_{\mathbf{k}}^\dagger = (\hat{c}_{\mathbf{k}1}^\dagger \quad \hat{c}_{\mathbf{k}2}^\dagger \quad \hat{c}_{\mathbf{k}3}^\dagger \quad \hat{c}_{\mathbf{k}4}^\dagger)$. The generalized C_4 symmetry takes the following form:

$$S_1^\dagger H(\mathbf{k}) S_1 = H(g\mathbf{k}'), \tag{A4}$$

where $\mathbf{k}' = (k_x, k_y - \pi)$ and

$$S_1 = \begin{pmatrix} 0 & 0 & 1 & 0 \\ -1 & 0 & 0 & 0 \\ 0 & 0 & 0 & 1 \\ 0 & 1 & 0 & 0 \end{pmatrix}. \tag{A5}$$

APPENDIX B: EQUIVALENCE BETWEEN OUR MODEL AND THE DISORDERED BBH MODEL

In this Appendix, we will prove that our model is equivalent to the BBH model in topological and localization properties. The BBH model reads

$$\hat{\tilde{H}} = \sum_{\mathbf{r}} [\hat{c}_{\mathbf{r}}^\dagger \tilde{h}_0 \hat{c}_{\mathbf{r}} + (\hat{c}_{\mathbf{r}}^\dagger h_x \hat{c}_{\mathbf{r}+\mathbf{e}_x} + \hat{c}_{\mathbf{r}}^\dagger h_y \hat{c}_{\mathbf{r}+\mathbf{e}_y} + \text{H.c.})], \tag{B1}$$

where $\tilde{h}_0$ is a real matrix expressed as

$$\tilde{h}_0 = \begin{pmatrix} 0 & m_{\mathbf{r}}^y & m_{\mathbf{r}}^x & 0 \\ m_{\mathbf{r}}^y & 0 & 0 & -\bar{m}_{\mathbf{r}}^x \\ m_{\mathbf{r}}^x & 0 & 0 & \bar{m}_{\mathbf{r}}^y \\ 0 & -\bar{m}_{\mathbf{r}}^x & \bar{m}_{\mathbf{r}}^y & 0 \end{pmatrix}. \tag{B2}$$

This model respects the time-reversal, particle-hole, and chiral symmetries.

While the two Hamiltonians have different symmetries, they are closely related by a local transformation $U_{\mathbf{r}} = \text{diag}(i^{x+y-1}, i^{x+y}, i^{x+y}, i^{x+y+1})$, that is, $U_{\mathbf{r}}^\dagger h_0 U_{\mathbf{r}} = \tilde{h}_0$, $U_{\mathbf{r}}^\dagger h_x U_{\mathbf{r}+\mathbf{e}_x} = h_x$, and $U_{\mathbf{r}}^\dagger h_y U_{\mathbf{r}+\mathbf{e}_y} = h_y$. Specifically, one can transform $\hat{H}$ in Eq. (1) to $\hat{\tilde{H}}$ by the transformation $\hat{c}_{\mathbf{r}} \rightarrow U_{\mathbf{r}} \hat{c}_{\mathbf{r}}$. In other words, if $\Psi_{E_i,\mathbf{r}\nu}$ is a spatial eigenstate of H, then $\tilde{\Psi}_{E_i,\mathbf{r}\nu} = (-i)^{f_{\mathbf{r}\nu}} \Psi_{E_i,\mathbf{r}\nu}$ with $f_{\mathbf{r}1} = x + y - 1$, $f_{\mathbf{r}2} = f_{\mathbf{r}3} = x + y$, and $f_{\mathbf{r}4} = x + y + 1$ is an eigenstate of $\tilde{H}$ corresponding to the same energy E_i. Here H and $\tilde{H}$ are the first-quantization Hamiltonians of $\hat{H}$ and $\hat{\tilde{H}}$, respectively. Therefore, $\hat{H}$ and $\hat{\tilde{H}}$ have the same energy spectrum and density profiles, indicating identical localization properties that they possess. In addition, this local phase transformation does not change the topological property, and thus the two Hamiltonians have the same topology. Under open boundary conditions, the two models are connected by the transformation irrelevant of the system size. Yet, under periodic boundary conditions, the transformation works well only when L_x and L_y are integer multiples of 4. For the topological property, the two models should be equivalent irrelevant of a system size given that the topology does not depend on a specific system size. For the localization property, we have also calculated the IPR and LSR of the two Hamiltonians with their sizes being odd and find similar results, showing that their localization properties are irrelevant of the parity of a system size.

APPENDIX C: QUANTIZATION OF QUADRUPOLE MOMENTS BY CHIRAL SYMMETRY

In this Appendix, we will prove that the quadrupole moment is protected to be quantized by chiral symmetry and thus can be used as a topological invariant. Note that the quadrupole moment may not characterize the physical quadrupole moment; we here are only interested in the formula as a topological invariant. We consider the quadrupole moment defined by [44,45]

$$\begin{aligned} q_{xy} &\equiv \left[\tilde{q}_{xy} - q_{xy}^{(0)}\right] \mod 1 \\ &= \left[\frac{1}{2\pi}\mathrm{Im}\log\langle\Psi_G|e^{2\pi i\hat{Q}_{xy}}|\Psi_G\rangle - q_{xy}^{(0)}\right] \mod 1, \end{aligned} \tag{C1}$$

where $\hat{Q}_{xy} = \sum_{j=1}^{n_c}\hat{x}_j\hat{y}_j/(L_xL_y)$ with $\hat{x}_j$ ($\hat{y}_j$) denoting the x-position (y-position) operator for electron j with $n_c = 2L_xL_y$ (the number of occupied states in our model) at half filling, and $|\Psi_G\rangle$ is the many-body ground state of electrons in the system. Here $\tilde{q}_{xy} = \frac{1}{2\pi}\mathrm{Im}[\log\langle\Psi_G|e^{2\pi i\hat{Q}_{xy}}|\Psi_G\rangle]$ is the contribution from occupied electrons, and

$$q_{xy}^{(0)} = \frac{1}{2}\sum_{j=1}^{n_a}x_jy_j/(L_xL_y) \tag{C2}$$

is the contribution from the background positive charge distribution where (x_j, y_j) denotes the position of the jth atomic orbital. Here, n_a is the total number of atomic orbitals so that the single-particle Hamiltonian is an $n_a \times n_a$ matrix. At half filling, $n_a = 2n_c$.

Let us write the many-body wave function of occupied electrons in real-space representation as

$$\begin{aligned} &\Psi_G(\mathbf{r}_1\nu_1, \mathbf{r}_2\nu_2, \cdots, \mathbf{r}_{n_c}\nu_{n_c}) \\ &= \frac{1}{\sqrt{n_c!}}\begin{vmatrix} \psi_1(\mathbf{r}_1\nu_1) & \psi_2(\mathbf{r}_1\nu_1) & \cdots & \psi_{n_c}(\mathbf{r}_1\nu_1) \\ \psi_1(\mathbf{r}_2\nu_2) & \psi_2(\mathbf{r}_2\nu_2) & \cdots & \psi_{n_c}(\mathbf{r}_2\nu_2) \\ \vdots & \vdots & \ddots & \vdots \\ \psi_1(\mathbf{r}_{n_c}\nu_{n_c}) & \psi_2(\mathbf{r}_{n_c}\nu_{n_c}) & \cdots & \psi_{n_c}(\mathbf{r}_{n_c}\nu_{n_c}) \end{vmatrix}, \end{aligned} \tag{C3}$$

where ψ_n represents the nth occupied eigenstate of a first-quantization Hamiltonian. Then, the quadrupole moment of occupied electrons, $\tilde{q}_{xy}$, can be evaluated through

$$\tilde{q}_{xy} = \frac{1}{2\pi}\mathrm{Im}\log\langle\Psi_G|\tilde{\Psi}_G\rangle, \tag{C4}$$

where

$$\langle\Psi_G|\tilde{\Psi}_G\rangle = \begin{vmatrix} \langle\psi_1|\tilde{\psi}_1\rangle & \langle\psi_1|\tilde{\psi}_2\rangle & \cdots & \langle\psi_1|\tilde{\psi}_{n_c}\rangle \\ \langle\psi_2|\tilde{\psi}_1\rangle & \langle\psi_2|\tilde{\psi}_2\rangle & \cdots & \langle\psi_2|\tilde{\psi}_{n_c}\rangle \\ \vdots & \vdots & \ddots & \vdots \\ \langle\psi_{n_c}|\tilde{\psi}_1\rangle & \langle\psi_{n_c}|\tilde{\psi}_2\rangle & \cdots & \langle\psi_{n_c}|\tilde{\psi}_2\rangle \end{vmatrix}, \tag{C5}$$

$\tilde{\psi}_n(\mathbf{r}\nu) = e^{i2\pi xy/(L_xL_y)}\psi_n(\mathbf{r}\nu)$, and $\langle\psi_m|\tilde{\psi}_n\rangle = \sum_{\mathbf{r}\alpha}\psi_m^*(\mathbf{r}\alpha)\tilde{\psi}_n(\mathbf{r}\alpha)$. Let us define $U_o = (|\psi_1\rangle, |\psi_2\rangle, \dots, |\psi_{n_c}\rangle)$ which is an $n_a \times n_c$ matrix representing the occupied states of electrons. Then we can express the quadrupole moment of occupied electrons as

$$\tilde{q}_{xy} = \frac{1}{2\pi}\mathrm{Im}\log\det(U_o^\dagger\hat{D}U_o), \tag{C6}$$

where we define an $n_a \times n_a$ diagonal matrix $\hat{D} = \mathrm{diag}\{e^{2\pi ix_jy_j/(L_xL_y)}\}_{j=1}^{n_a}$ with (x_j, y_j) denoting the position of the jth atomic orbital.

For a generic Hamiltonian in real space, H, with chiral (sublattice) symmetry, $\Pi H\Pi^{-1} = -H$, if $|\psi_n\rangle$ is an eigenstate of H corresponding to energy E_n, $\Pi|\psi_n\rangle$ is also an eigenstate of H with energy $-E_n$, corresponding to an unoccupied state. The set $\{\Pi|\psi_1\rangle, \Pi|\psi_2\rangle, \dots, \Pi|\psi_{n_c}\rangle\}$ therefore constitutes the unoccupied states. We then define $U_u = (\Pi|\psi_1\rangle, \Pi|\psi_2\rangle, \dots, \Pi|\psi_{n_c}\rangle) = \Pi U_o$ representing the unoccupied states of electrons. The quadrupole moment $\tilde{q}_{xy}^u$ for the unoccupied states is

$$\tilde{q}_{xy}^u = \frac{1}{2\pi}\mathrm{Im}\log\det(U_u^\dagger\hat{D}U_u) \tag{C7}$$

$$= \frac{1}{2\pi}\mathrm{Im}\log\det(U_o^\dagger\Pi^\dagger\hat{D}\Pi U_o). \tag{C8}$$

Clearly, $\hat{D}$ commutes with the chiral (sublattice) symmetry transformation Π, i.e., $[\hat{D}, \Pi] = 0$,

$$\tilde{q}_{xy}^u = \frac{1}{2\pi}\mathrm{Im}\log\det(U_o^\dagger\hat{D}U_o) = \tilde{q}_{xy}. \tag{C9}$$

Let us define $q_{xy}^u \equiv [\tilde{q}_{xy}^u - q_{xy}^{(0)}] \mod 1$. Then we will have

$$q_{xy}^u = \left[\tilde{q}_{xy} - q_{xy}^{(0)}\right] \mod 1 = q_{xy}. \tag{C10}$$

Next we will prove that $q_{xy} + q_{xy}^u = 0 \mod 1$, i.e., $\tilde{q}_{xy} + \tilde{q}_{xy}^u - 2q_{xy}^{(0)} = 0 \mod 1$.

Proof. We define a unitary matrix $U_t = (U_o, U_u)$. It can be easily seen that

$$2q_{xy}^{(0)} = \sum_{j=1}^{n_a}x_jy_j/(L_xL_y) \tag{C11}$$

$$= \frac{1}{2\pi}\mathrm{Im}\log\det\hat{D} \mod 1 \tag{C12}$$

$$= \frac{1}{2\pi}\mathrm{Im}\log\det(U_t^\dagger\hat{D}U_t) \mod 1. \tag{C13}$$

Then we have the following relations:

$$\begin{aligned} &2\pi\left(-\tilde{q}_{xy} - \tilde{q}_{xy}^u + 2q_{xy}^{(0)}\right) \\ &= -\mathrm{Im}\log\det(U_o^\dagger\hat{D}U_o) - \mathrm{Im}\log\det(U_u^\dagger\hat{D}U_u) \\ &\quad +\mathrm{Im}\log\det(U_t^\dagger\hat{D}U_t) \\ &= \mathrm{Im}\log\det(U_o^\dagger\hat{D}^\dagger U_o) + \mathrm{Im}\log\det(U_u^\dagger\hat{D}^\dagger U_u) \\ &\quad +\mathrm{Im}\log\det\begin{pmatrix} U_o^\dagger DU_o & U_o^\dagger\hat{D}U_u \\ U_u^\dagger DU_o & U_u^\dagger\hat{D}U_u \end{pmatrix} \\ &= \mathrm{Im}\log\det\begin{pmatrix} U_o^\dagger\hat{D}^\dagger U_o & U_o^\dagger\hat{D}^\dagger U_u \\ 0 & U_u^\dagger\hat{D}^\dagger U_u \end{pmatrix} \\ &\quad +\mathrm{Im}\log\det\begin{pmatrix} U_o^\dagger\hat{D}U_o & U_o^\dagger\hat{D}U_u \\ U_u^\dagger\hat{D}U_o & U_u^\dagger\hat{D}U_u \end{pmatrix} \\ &= \mathrm{Im}\log\det\left[\begin{pmatrix} U_o^\dagger\hat{D}^\dagger U_o & U_o^\dagger\hat{D}^\dagger U_u \\ 0 & U_u^\dagger\hat{D}^\dagger U_u \end{pmatrix}\begin{pmatrix} U_o^\dagger\hat{D}U_o & U_o^\dagger\hat{D}U_u \\ U_u^\dagger\hat{D}U_o & U_u^\dagger\hat{D}U_u \end{pmatrix}\right] \\ &= \mathrm{Im}\log\det\begin{pmatrix} \mathbb{1} & 0 \\ U_u^\dagger\hat{D}^\dagger U_uU_u^\dagger\hat{D}U_o & U_u^\dagger\hat{D}^\dagger U_uU_u^\dagger\hat{D}U_u \end{pmatrix} \end{aligned}$$

$$\begin{aligned}&= \operatorname{Im}\log\det(U_u^\dagger \hat{D}^\dagger U_u U_u^\dagger \hat{D} U_u)\\ &= \operatorname{Im}\log\det(U_u^\dagger \hat{D} U_u)^\dagger + \operatorname{Im}\log\det(U_u^\dagger \hat{D} U_u)\\ &= 0 \mod 2\pi. \end{aligned} \tag{C14}$$

In the derivation, we have utilized the orthonormal properties $U_o^\dagger U_o = U_u^\dagger U_u = \mathbb{1}$, $U_o^\dagger U_u = 0$, and $U_o U_o^\dagger + U_u U_u^\dagger = \mathbb{1}$. ■

Therefore, we have the following relation:

$$q_{xy} + q_{xy}^u = 0 \mod 1. \tag{C15}$$

Combined with the relation that $q_{xy}^u = q_{xy}$, we get the conclusion that $2q_{xy} = 0 \mod 1$, namely, q_{xy} is quantized to zero or 0.5 up to an integer. The result is consistent with our numerical results where all disorder configurations exhibit quantized quadrupole moments. We note that this proof remains valid when we replace $\hat{Q}_{xy}$ and $q_{xy}^{(0)}$ in the definition of q_{xy} with $\hat{Q}_f = \sum_{j=1}^{n_c} f(\hat{x}_j, \hat{y}_j)$ and $q_f^{(0)} = \frac{1}{2}\sum_{j=1}^{n_a} f(x_j, y_j)$, respectively, where $f(x, y)$ is a general real function, so that the newly defined quantity is also quantized by chiral symmetry like the quadrupole moment. In addition, one can use the same procedure to prove the quantization of the octupole moment in three dimensions protected by chiral symmetry.

We note that while we have proved that the quadrupole moment is quantized to either zero or 0.5 for each disorder configuration protected by chiral symmetry, for a disorder system, we need to consider many distinct samples and perform the average of the quadrupole moment over these samples. In this case, the averaged quadrupole moment may not be quantized since for some samples the quadruple moments are equal to 0.5 and for others they are equal to zero when a system size is not large as shown in Fig. 9.

It is worth mentioning that Ref. [19] has found that quadrupole topological insulators with quantized quadrupole moments can still exist even in amorphous systems without crystalline symmetries. We now can understand that the quantized quadrupole moment found in Ref. [19] is protected by chiral symmetry.

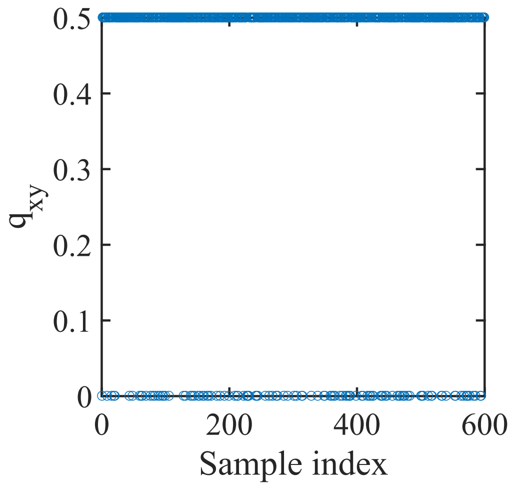

FIG. 9. The quadrupole moment q_{xy} for different disorder configurations when $W = 2.6$, showing that $q_{xy} = 0.5$ for most disorder samples and $q_{xy} = 0$ for others. Here $L_x = L_y = 80$ and $m_x = m_y = 1.1$.

APPENDIX D: EFFECTIVE BOUNDARY HAMILTONIAN

In this section, we follow the transfer matrix method introduced in Ref. [48] to derive the effective boundary Hamiltonian of our system in the clean case. We will show that the effective boundary Hamiltonian at the y-normal (x-normal) edges is proportional to $H_x(k_x, m_x)$ [$H_y(k_y, m_y)$] up to a nonzero factor, implying that the higher-order topology can be characterized by the topological invariant P introduced in the main text.

Specifically, let us write the Hamiltonian as $\hat{H} = \hat{c}^\dagger H \hat{c}$ where $\hat{c}^\dagger = (\hat{c}_1^\dagger \quad \hat{c}_2^\dagger \quad \cdots \quad \hat{c}_{L_y}^\dagger)$ with the index j denoting the jth layer consisting of sites along x and H reads

$$H = \begin{pmatrix} h_1 & V_1^\dagger & 0 & 0 & 0 & \cdots & 0\\ V_1 & h_2 & V_2^\dagger & 0 & 0 & \cdots & 0\\ 0 & V_2 & h_3 & V_3^\dagger & 0 & \cdots & 0\\ 0 & 0 & V_3 & h_4 & V_4^\dagger & \cdots & 0\\ \vdots & \vdots & \vdots & \ddots & \ddots & \ddots & \vdots\\ 0 & 0 & 0 & \cdots & V_{2L_y-2} & h_{2L_y-1} & V_{2L_y-1}^\dagger\\ 0 & 0 & 0 & \cdots & 0 & V_{2L_y-1} & h_{2L_y} \end{pmatrix} \tag{D1}$$

with V_n denoting the coupling between the nth and $(n+1)$th layer. In disordered systems, the parameters in h_n and V_{2n-1} describing the intracell hopping are randomly generated.

In the clean case, the system has the translational invariance of period 2 and thus there are two different layers described by the Hamiltonian, h_1 and h_2, respectively. If we view these two layers as a unit cell, we use V_1 and V_2 to describe the intracell and intercell layer coupling, respectively. Now H can be simplified as

$$H = \begin{pmatrix} h_1 & V_1^\dagger & 0 & 0 & 0 & \cdots & 0\\ V_1 & h_2 & V_2^\dagger & 0 & 0 & \cdots & 0\\ 0 & V_2 & h_1 & V_1^\dagger & 0 & \cdots & 0\\ 0 & 0 & V_1 & h_2 & V_2^\dagger & \cdots & 0\\ \vdots & \vdots & \vdots & \ddots & \ddots & \ddots & \vdots\\ 0 & 0 & 0 & \cdots & V_2 & h_1 & V_1^\dagger\\ 0 & 0 & 0 & \cdots & 0 & V_1 & h_2 \end{pmatrix}. \tag{D2}$$

Considering the periodic boundaries along x, we write h_1, h_2, V_1, and V_2 in momentum space as $h_1 = -h_2 = H_x(k_x, m_x)$, $V_1 = i m_y \sigma_0$, and $V_2 = \sigma_0$. When $m_y = 0$, it is clear to see that the effective boundary Hamiltonian is $H_x(k_x, m_x)$. When $m_y \neq 0$, we obtain the following two transfer matrices at energy E:

$$\begin{aligned} M_1(E) &= \begin{pmatrix} i(E\sigma_0 - h_1)/m_y & -i\sigma_0/m_y\\ \sigma_0 & 0_{2\times 2} \end{pmatrix},\\ M_2(E) &= \begin{pmatrix} (E\sigma_0 - h_2) & -i m_y \sigma_0\\ \sigma_0 & 0_{2\times 2} \end{pmatrix}, \end{aligned} \tag{D3}$$

where the transfer matrices connect the eigenstate in neighboring layers through

$$\begin{aligned} \begin{pmatrix} \Psi_{2n}\\ \Psi_{2n-1} \end{pmatrix} &= M_1 \begin{pmatrix} \Psi_{2n-1}\\ \Psi_{2n-2} \end{pmatrix},\\ \begin{pmatrix} \Psi_{2n+1}\\ \Psi_{2n} \end{pmatrix} &= M_2 \begin{pmatrix} \Psi_{2n}\\ \Psi_{2n-1} \end{pmatrix}, \end{aligned} \tag{D4}$$

with $n \geqslant 1$ and Ψ_n is the component in the nth layer of an eigenstate with the energy E.

We now define the total transfer matrix at zero energy as

$$T = M_2(E=0)M_1(E=0) = -\frac{i}{m_y}\begin{pmatrix} A(k_x)\sigma_0 & h_1 \\ h_1 & \sigma_0 \end{pmatrix}, \quad \text{(D5)}$$

where $A(k_x) = 1 + m_x^2 + m_y^2 + 2m_x \sin k_x$. This matrix can be reduced to a diagonal block form through an elementary interchange transformation,

$$S_{24}TS_{24} = -\frac{i}{m_y}\begin{pmatrix} H_1 & 0_{2\times2} \\ 0_{2\times2} & H_2 \end{pmatrix}, \quad \text{(D6)}$$

where

$$S_{24} = \begin{pmatrix} 1 & 0 & 0 & 0 \\ 0 & 0 & 0 & 1 \\ 0 & 0 & 1 & 0 \\ 0 & 1 & 0 & 0 \end{pmatrix},$$

$$H_1 = \begin{pmatrix} A(k_x) & -im_x + e^{-ik_x} \\ im_x + e^{ik_x} & 1 \end{pmatrix}, \quad \text{(D7)}$$

$$H_2 = \begin{pmatrix} 1 & -im_x + e^{-ik_x} \\ im_x + e^{ik_x} & A(k_x) \end{pmatrix}.$$

Evidently, H_1 and H_2 have the same eigenvalues. Since T is a symplectic matrix, its eigenvalues show up in pairs as $(\lambda, 1/\lambda^*)$. Suppose that $\lambda_1 m_y$ ($|\lambda_1| > 1$) is an eigenvalue of H_1; then

$$\begin{aligned} TU &= T\begin{pmatrix} U_{11} & U_{12} \\ U_{21} & U_{22} \end{pmatrix} \\ &= -i\begin{pmatrix} U_{11} & U_{12} \\ U_{21} & U_{22} \end{pmatrix}\begin{pmatrix} \lambda_1\sigma_0 & 0_{2\times2} \\ 0_{2\times2} & \sigma_0/\lambda_1^* \end{pmatrix}, \end{aligned} \quad \text{(D8)}$$

where U is made up of eigenvectors of H_1 and H_2. Then, the fixed-point boundary Green's function is given by

$$G(E=0) = \lim_{N\to\infty} G_N(E=0) = U_{21}(U_{11})^{-1}(V_0^\dagger)^{-1}, \quad \text{(D9)}$$

where V_0 can be chosen as any invertible matrix. By calculating eigenvectors of H_1 and H_2, we obtain the effective boundary Hamiltonian along x,

$$H_{\text{eff}}(k_x) = -G(E=0)^{-1} = \frac{g(k_x)}{f(k_x)}H_x(k_x, m_x), \quad \text{(D10)}$$

where $g(k_x) = -(m_y\lambda_1 - 1)$ and $f(k_x) = 1 + m_x^2 + 2m_x \sin k_x \geqslant (1 - |m_x|)^2 > 0$ ($m_x = 1$ is not considered as it corresponds to a phase boundary). Let us further prove that $g(k_x) < 0$ for all k_x. Suppose $m_y > 0$; then $\lambda_1 = \frac{1}{2m_y}[A(k_x) + 1 + \sqrt{(A(k_x)+1)^2 - 4m_y^2}]$, and we have

$$\begin{aligned} 2g(k_x) &= -A(k_x) + 1 - \sqrt{(A(k_x)+1)^2 - 4m_y^2} \\ &\leqslant -(m_y^2 + m_x^2 - 2|m_x|) \\ &\quad -\sqrt{[1 + m_y^2 + (1 - m_x)^2] - 4m_y^2} \\ &< -\big(m_y^2 + m_x^2 - 2|m_x|\big) \\ &\quad -\big|1 - m_y^2 + (1 - |m_x|)^2\big|, \end{aligned} \quad \text{(D11)}$$

where we have used $A(k_x) \geqslant (1 - |m_x|)^2 + m_y^2$. If $1 - m_y^2 + (1 - |m_x|)^2 > 0$, then $g(k_x) < -(1 - |m_x|)^2 < 0$; otherwise, we have $m_y^2 + m_x^2 - 2m_x > 2(1 - |m_x|)^2 > 0$, giving $g(k_x) < 0$. Similarly,

$$H_{\text{eff}}(k_y) = \frac{\bar{g}(k_y)}{\bar{f}(k_y)}H_y(k_y, m_y), \quad \text{(D12)}$$

where $\bar{g}(k_y) = -(m_x\lambda_2 + 1)$ and $\bar{f}(k_y) = 1 + m_y^2 + 2m_y \sin k_y$ with $\lambda_2 = -\frac{1}{2m_x}[B(k_y) + 1 + \sqrt{(B(k_y)+1)^2 - 4m_x^2}]$ and $B(k_y) = 1 + m_x^2 + m_y^2 + 2m_y \sin k_y$.

Evidently, the higher-order topological phase arises when these effective boundary Hamiltonians become topological and thus can be characterized by the topological invariant P.

APPENDIX E: GRIFFITHS REGIME

In the main text, we have shown the existence of a Griffiths phase where topologically nontrivial and trivial samples coexist, leading to the topological invariant P that is not quantized. In Fig. 10, we plot the polarizations in 200 different iteration steps corresponding to different sample configurations. We see that, in the Griffiths regime, some results show the polarization of 0.5 and others zero.

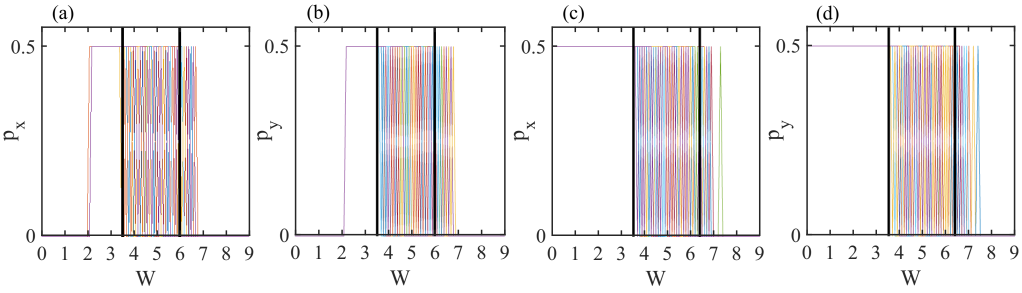

FIG. 10. The polarizations [(a),(c)] p_x and [(b),(d)] p_y for the 801st to 1000th iterations corresponding to different disorder configurations. The region between two vertical lines correspond to the Griffiths regime. [(a),(b)] $m_x = m_y = 1.1$ and [(c),(d)] $m_x = m_y = 0.5$. Here $L_x = L_y = 500$.

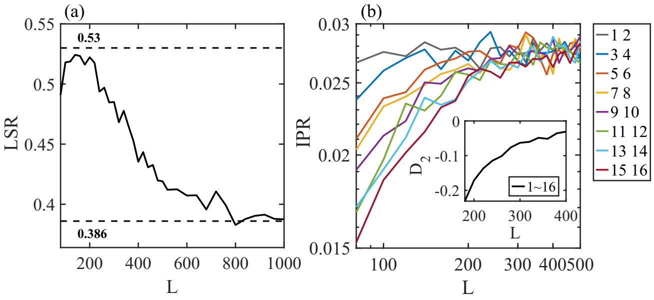

FIG. 11. (a) The LSR with respect to the system size L for $W = 1$ and (b) the IPR with respect to the system size L for $W = 3.2$ for different energy levels around zero energy. The inset shows the fractal dimension D_2 averaged over these energy levels as a function of L. Here $m_x = m_y = 1.1$.

APPENDIX F: THE FINITE-SIZE ANALYSIS OF THE LSR AND IPR

In the main text, we have shown that the LSR at the band edge around zero energy in the region around $W = 1$ is close to 0.386, indicating that the states are localized. Here we further plot the LSR for $W = 1$ with respect to the system size in Fig. 11(a), illustrating that the LSR approaches 0.386 as the system size increases. We have also shown in the main text that for the localized states, the fractal dimension D_2 can take negative values due to finite-size effects. Here we plot the IPR with respect to the system size in Fig. 11(b), showing the increase of the IPR with respect to the system size for a system with moderate sizes. Such an increase gives a negative fractal dimension. Yet, the increased slope declines as the system size is raised, indicating that D_2 approaches zero in the thermodynamic limit.

---

[1] W. A. Benalcazar, B. A. Bernevig, and T. L. Hughes, Quantized electric multipole insulators, Science **357**, 61 (2017).

[2] M. Sitte, A. Rosch, E. Altman, and L. Fritz, Topological Insulators in Magnetic Fields: Quantum Hall Effect and Edge Channels with a Nonquantized θ Term, Phys. Rev. Lett. **108**, 126807 (2012).

[3] F. Zhang, C. L. Kane, and E. J. Mele, Surface State Magnetization and Chiral Edge States on Topological Insulators, Phys. Rev. Lett. **110**, 046404 (2013).

[4] R.-J. Slager, L. Rademaker, J. Zaanen, and L. Balents, Impurity-bound states and Green's function zeros as local signatures of topology, Phys. Rev. B **92**, 085126 (2015).

[5] Z. Song, Z. Fang, and C. Fang, $(d-2)$-Dimensional Edge States of Rotation Symmetry Protected Topological States, Phys. Rev. Lett. **119**, 246402 (2017).

[6] J. Langbehn, Y. Peng, L. Trifunovic, F. von Oppen, and P. W. Brouwer, Reflection-Symmetric Second-Order Topological Insulators and Superconductors, Phys. Rev. Lett. **119**, 246401 (2017).

[7] F. Schindler, A. M. Cook, M. G. Vergniory, Z. Wang, S. S. P. Parkin, B. A. Bernevig, and T. Neupert, Higher-order topological insulators, Sci. Adv. **4**, eaat0346 (2018).

[8] L. Trifunovic and P. W. Brouwer, Higher-Order Bulk-Boundary Correspondence for Topological Crystalline Phases, Phys. Rev. X **9**, 011012 (2019).

[9] D. Călugăru, V. Juričić, and B. Roy, Higher-order topological phases: A general principle of construction, Phys. Rev. B **99**, 041301(R) (2019).

[10] X.-L. Sheng, C. Chen, H. Liu, Z. Chen, Z.-M. Yu, Y. X. Zhao, and S. A. Yang, Two-Dimensional Second-Order Topological Insulator in Graphdiyne, Phys. Rev. Lett. **123**, 256402 (2019).

[11] B. Huang and W. V. Liu, Floquet Higher-Order Topological Insulators with Anomalous Dynamical Polarization, Phys. Rev. Lett. **124**, 216601 (2020).

[12] H. Hu, B. Huang, E. Zhao, and W. V. Liu, Dynamical Singularities of Floquet Higher-Order Topological Insulators, Phys. Rev. Lett. **124**, 057001 (2020).

[13] Y.-B. Yang, K. Li, L.-M. Duan, and Y. Xu, Type-II quadrupole topological insulators, Phys. Rev. Res. **2**, 033029 (2020).

[14] A. Tiwari, M.-H. Li, B. A. Bernevig, T. Neupert, and S. A. Parameswaran, Unhinging the Surfaces of Higher-Order Topological Insulators and Superconductors, Phys. Rev. Lett. **124**, 046801 (2020).

[15] H. Araki, T. Mizoguchi, and Y. Hatsugai, Phase diagram of a disordered higher-order topological insulator: A machine learning study, Phys. Rev. B **99**, 085406 (2019).

[16] Z. Su, Y. Kang, B. Zhang, Z. Zhang, and H. Jiang, Disorder induced phase transition in magnetic higher-order topological insulator: A machine learning study, Chin. Phys. B **28**, 117301 (2019).

[17] S. Franca, D. V. Efremov, and I. C. Fulga, Phase-tunable second-order topological superconductor, Phys. Rev. B **100**, 075415 (2019).

[18] C.-A. Li and S.-S. Wu, Topological states in generalized electric quadrupole insulators, Phys. Rev. B **101**, 195309 (2020).

[19] A. Agarwala, V. Juričić, and B. Roy, Higher-order topological insulators in amorphous solids, Phys. Rev. Res. **2**, 012067(R) (2020).

[20] C. Wang and X. R. Wang, Disorder-induced quantum phase transitions in three-dimensional second-order topological insulators, Phys. Rev. Res. **2**, 033521 (2020).

[21] F. Evers and A. D. Mirlin, Anderson transitions, Rev. Mod. Phys. **80**, 1355 (2008).

[22] J. Li, R.-L. Chu, J. K. Jain, and S.-Q. Shen, Topological Anderson Insulator, Phys. Rev. Lett. **102**, 136806 (2009).

[23] C. W. Groth, M. Wimmer, A. R. Akhmerov, J. Tworzydło, and C. W. J. Beenakker, Theory of the Topological Anderson Insulator, Phys. Rev. Lett. **103**, 196805 (2009).

[24] H. Jiang, L. Wang, Q.-F. Sun, and X. C. Xie, Numerical study of the topological Anderson insulator in HgTe/CdTe quantum wells, Phys. Rev. B **80**, 165316 (2009).

[25] H.-M. Guo, G. Rosenberg, G. Refael, and M. Franz, Topological Anderson Insulator in Three Dimensions, Phys. Rev. Lett. **105**, 216601 (2010).

[26] A. Altland, D. Bagrets, L. Fritz, A. Kamenev, and H. Schmiedt, Quantum Criticality of Quasi-One-Dimensional Topological Anderson Insulators, Phys. Rev. Lett. **112**, 206602 (2014).

[27] I. Mondragon-Shem, T. L. Hughes, J. Song, and E. Prodan, Topological Criticality in the Chiral-Symmetric AIII Class at Strong Disorder, Phys. Rev. Lett. **113**, 046802 (2014).

[28] P. Titum, N. H. Lindner, M. C. Rechtsman, and G. Refael, Disorder-Induced Floquet Topological Insulators, Phys. Rev. Lett. **114**, 056801 (2015).

[29] C. Liu, W. Gao, B. Yang, and S. Zhang, Disorder-Induced Topological State Transition in Photonic Metamaterials, Phys. Rev. Lett. **119**, 183901 (2017).

[30] C.-Z. Chen, J. Song, H. Jiang, Q.-F. Sun, Z. Wang, and X. C. Xie, Disorder and Metal-Insulator Transitions in Weyl Semimetals, Phys. Rev. Lett. **115**, 246603 (2015).

[31] S. Stützer, Y. Plotnik, Y. Lumer, P. Titum, N. H. Lindner, M. Segev, M. C. Rechtsman, and A. Szameit, Photonic topological Anderson insulators, Nature (London) **560**, 461 (2018).

[32] E. J. Meier, F. A. An, A. Dauphin, M. Maffei, P. Massignan, T. L. Hughes, and B. Gadway, Observation of the topological Anderson insulator in disordered atomic wires, Science **362**, 929 (2018).

[33] A. Altland and M. R. Zirnbauer, Nonstandard symmetry classes in mesoscopic normal-superconducting hybrid structures, Phys. Rev. B **55**, 1142 (1997).

[34] C. W. J. Beenakker, Random-matrix theory of quantum transport, Rev. Mod. Phys. **69**, 731 (1997).

[35] F. Haake, *Quantum Signatures of Chaos* (Springer-Verlag, Berlin, 2006).

[36] S. Ryu, A. P. Schnyder, A. Furusaki, and A. W. W. Ludwig, Topological insulators and superconductors: Tenfold way and dimensional hierarchy, New J. Phys. **12**, 065010 (2010).

[37] F. J. Dyson, The dynamics of a disordered linear chain, Phys. Rev. **92**, 1331 (1953).

[38] G. Theodorou and M. H. Cohen, Extended states in a one-dimensional system with off-diagonal disorder, Phys. Rev. B **13**, 4597 (1976).

[39] T. P. Eggarter and R. Riedinger, Singular behavior of tight-binding chains with off-diagonal disorder, Phys. Rev. B **18**, 569 (1978).

[40] A. Eilmes, R. A. Römer, and M. Schreiber, The two-dimensional Anderson model of localization with random hopping, Eur. Phys. J. B **1**, 29 (1998).

[41] P. W. Brouwer, C. Mudry, B. D. Simons, and A. Altland, Delocalization in Coupled One-Dimensional Chains, Phys. Rev. Lett. **81**, 862 (1998).

[42] R. Okugawa, S. Hayashi, and T. Nakanishi, Second-order topological phases protected by chiral symmetry, Phys. Rev. B **100**, 235302 (2019).

[43] Q.-B. Zeng, Y.-B. Yang, and Y. Xu, Higher-order topological insulators and semimetals in generalized Aubry-André-Harper models, Phys. Rev. B **101**, 241104(R) (2020).

[44] B. Kang, K. Shiozaki, and G. Y. Cho, Many-body order parameters for multipoles in solids, Phys. Rev. B **100**, 245134 (2019).

[45] W. A. Wheeler, L. K. Wagner, and T. L. Hughes, Many-body electric multipole operators in extended systems, Phys. Rev. B **100**, 245135 (2019).

[46] R. Resta, Quantum-Mechanical Position Operator in Extended Systems, Phys. Rev. Lett. **80**, 1800 (1998).

[47] X. Dai, T. L. Hughes, X.-L. Qi, Z. Fang, and S.-C. Zhang, Helical edge and surface states in HgTe quantum wells and bulk insulators, Phys. Rev. B **77**, 125319 (2008).

[48] Y. Peng, Y. Bao, and F. von Oppen, Boundary Green functions of topological insulators and superconductors, Phys. Rev. B **95**, 235143 (2017).

[49] V. Oganesyan and D. A. Huse, Localization of interacting fermions at high temperature, Phys. Rev. B **75**, 155111 (2007).

[50] C. Castellani and L. Peliti, Multifractal wavefunction at the localisation threshold, J. Phys. A **19**, L429 (1986).

[51] A. MacKinnon and B. Kramer, The scaling theory of electrons in disordered solids: Additional numerical results, Z. Phys. B **53**, 1 (1983).

[52] M. Serra-Garcia, V. Peri, R. Süsstrunk, O. R. Bilal, T. Larsen, L. G. Villanueva, and S. D. Huber, Observation of a phononic quadrupole topological insulator, Nature (London) **555**, 342 (2018).

[53] C. W. Peterson, W. A. Benalcazar, T. L. Hughes, and G. Bahl, A quantized microwave quadrupole insulator with topologically protected corner states, Nature (London) **555**, 346 (2018).

[54] S. Imhof, C. Berger, F. Bayer, J. Brehm, L. W. Molenkamp, T. Kiessling, F. Schindler, C. H. Lee, M. Greiter, T. Neupert, and R. Thomale, Topolectrical-circuit realization of topological corner modes, Nat. Phys. **14**, 925 (2018).

[55] S. Mittal, V. V. Orre, G. Zhu, M. A. Gorlach, A. Poddubny, and M. Hafezi, Photonic quadrupole topological phases, Nat. Photonics **13**, 692 (2019).

[56] C.-A. Li, B. Fu, Z.-A. Hu, J. Li, and S.-Q. Shen, Topological Phase Transitions in Disordered Electric Quadrupole Insulators, Phys. Rev. Lett. **125**, 166801 (2020).

[57] W. Zhang, D. Zou, Q. Pei, W. He, J. Bao, H. Sun, and X. Zhang, Experimental observation of higher-order topological Anderson insulators, arXiv:2008.00423.